Analysis and Design of a High-Performance Traction Motor for Heavy-Duty Vehicles

Dong-Kyu Lee and **Jong-Suk Ro** *

Department of Electronic and Electrical Engineering, Chung-Ang University, Seoul 06974, Korea; lielove0330@cau.ac.kr
* Correspondence: jongsukro@cau.ac.kr; Tel.: +82-010-9530-7911

check for updates

Abstract: Due to environmental issues and depletion of resources, global attentiveness in electric vehicles (EVs) is growing. In particular, research on high specification motors for driving large EVs has attracted a lot of attention. In this study, an analysis and design process for a motor that can be universally applied in heavy vehicles to reduce environmental pollution was introduced. Motors for driving heavy vehicles require high specifications. Thus, an interior permanent magnet synchronous motor (IPMSM) with a delta-shaped magnet array was used to improve the torque and power characteristics. A step skew rotor structure was also used to dampen vibration and noise by minimizing the high-order harmonics in the cogging torque. The proposed analysis and design approach also reduces the total harmonic distortion (THD) of the back electromotive force (EMF). The effectiveness of the proposed analysis and design process and the usefulness of the resulting high-performance traction motor for heavy-duty vehicles were verified via the finite element method (FEM) and by experiment.

Keywords: electric vehicles; finite-element method; interior permanent magnet synchronous motor; traction motor; heavy-duty vehicles

1. Introduction

Steadily worsening global environmental problems and the depletion of fossil fuel resources have increased the demand for electric vehicles (EVs). EVs replace conventional internal combustion engines with electric powertrain systems, leading to a reduction in the use of fossil fuels, lower emissions, and greater energy efficiency. Currently, the EV market for passenger cars is growing [1,2], but heavy-duty vehicles such as buses, trailers, and trucks need higher performance specifications, thus the electrification of these vehicles is still in the research phase.

Traction motors are a key component of EVs. Although traction motors for electric buses, trucks, and trailers are currently under development, this study focuses on the development of a motor that can be universally employed in a diverse range of heavy-duty vehicles, which could significantly reduce development costs and time. Electric motors for large vehicles need higher torque, higher power, and a broader range of driving speeds than those employed in normal passenger cars. Therefore, in this study, a motor was designed by analyzing existing reference models to meet the following goals: a maximum power of 250 kW, a maximum torque of 1200 Nm, and a maximum speed of 6000 rpm. We also attempted to reduce the total harmonic distortion (THD) of the back electromotive force (EMF) and the high-order harmonics of the cogging torque, which affect vibration and noise when the vehicle is in operation.

The developmental process of the present study follows a trial-and-error approach to produce the target performance. This is a common analysis method for motor design that can be employed to quickly achieve design objectives that are useful for both traction motors and other electric machines.

The most common traction motors used for EVs are induction motors and interior permanent magnet synchronous motors (IPMSMs). Heavy-duty EVs require high efficiency and high torque [3,4], but induction motors have the drawback of being less efficient than IPMSMs under urban driving conditions. The most significant advantage of IPMSMs is that it is easy to produce high torque because they simultaneously employ the torque produced by magnets and reluctance [5–7]. Surface permanent magnet synchronous motors (SPMSMs) also exhibit high torque but suffer from mechanical instability due to their structure [8]. Therefore, this study adopted an IPMSM due to its higher efficiency and more advantageous torque characteristics compared to other types of motor. We designed a delta-type IPMSM traction motor that maximized the reluctance torque with a delta-shaped magnet array in the rotor.

This delta-shaped magnet arrangement combines a bar-type magnetic array with a V-type magnetic array [9]. The bar-type array increases the magnetic flux along the d-axis, thus increasing the magnetic torque, while the V-type array increases the reluctance torque, raising the overall torque [10–14]. This magnetic arrangement can also concentrate the magnetic flux so that it is easy to obtain a sinusoidal back EMF waveform. In this study, we present a formula for calculating the step skew angle to remove the specific harmonic component that has the greatest influence on the back EMF and cogging torque in three-phase IPMSMs. It has been demonstrated that this can minimize the THD of the back EMF and the specific harmonics of the cogging torque [15]. In this research, we used JMAG software for finite element method (FEM) analysis.

2. Proposed Analysis and Design Method for a High-Performance Traction Motor for Heavy-Duty Vehicles

Figure 1 outlines the process for the design of the IPMSM traction motor for heavy-duty vehicles, which is described in detail in this section.
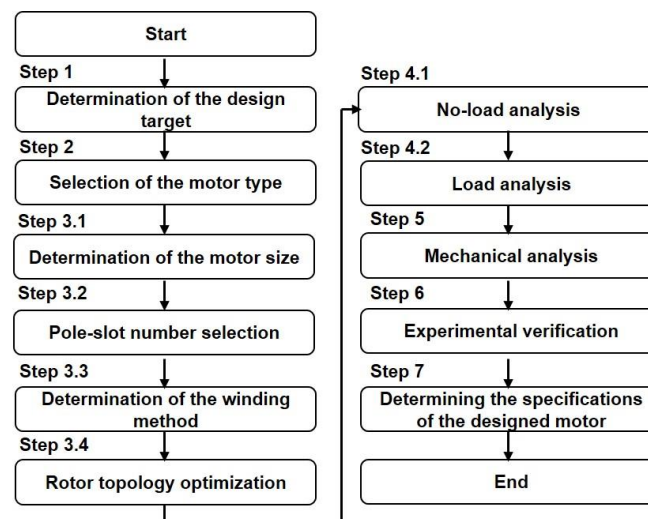

Figure 1. Proposed design process for the traction motor.

Step 1. Determination of the Design Target

Traction motors for large goods vehicles should have more advanced performance than the motors used in normal vehicles. Currently, the highest-performing traction motor for electric buses has a highest torque of 900 Nm, a highest power of 250 kW, and a maximum speed of 5500 rpm. Therefore, the objective of this study was to attain a peak torque, power, and speed of 1200 Nm, 250 kW, and 6000 rpm, respectively, by improving the motor performance.

Step 2. Selection of Motor Type

Two clear advantages of an IPMSM are its high torque and mechanical stability [16]. The torque of an IPMSM is expressed by Equation (1), where P represents the number of magnetic poles, φ_f represents the magnetic flux interlinkage provided by permanent magnets, i_q and i_d represent the q and d axis currents, respectively, and L_q and L_d represent the q and d axis inductances, respectively. The first term represents the torque generated by the magnets and the second term represents the reluctance torque. An IPMSM can be designed by considering the rotor's various features. In this study, a delta-shaped arrangement of magnets was used inside the rotor, as shown in Figure 2a. This delta arrangement combines a V-type magnetic array with straight bar-type magnets. The straight bar-type magnets of the delta-type IPMSM increase the magnetic flux in the direction of the d axis, thereby increasing the magnetic torque. Moreover, the V-type magnet array increases the inductance of the q axis by widening the flux path to increase the difference between the d axis and q axis inductances, thereby increasing the reluctance torque. Figure 2b presents the generated mesh grid of the motor for finite element method (FEM) analysis. When analyzing the characteristics of IPMSM, the flux saturation of core and leakage flux that varies non linearly as applied load changes should be considered. Therefore, a more accurate analysis requires a finer mesh grid in the rotor bridge ribs and stator teeth areas where magnetic saturation is severe when a current is applied [17–19].
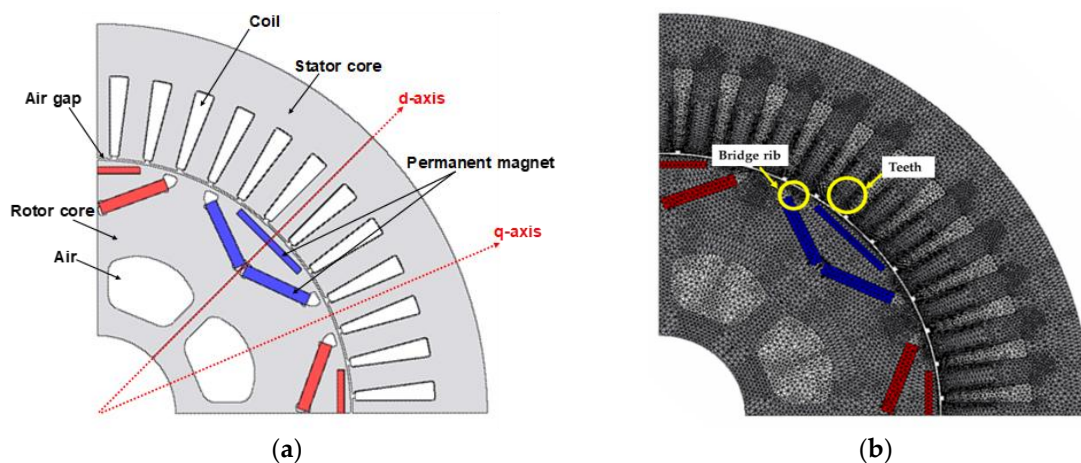

(**a**)   (**b**)

Figure 2. The structure of a designed motor for heavy vehicles: (**a**) the construction of the motor and (**b**) the finite element method (FEM) mesh grid for motor calculations.

The delta-type magnetic arrangement facilitates the concentration of magnetic flux in the q axis direction. This is advantageous for obtaining back EMF and air gap flux density in the form of sinusoidal waves:

$$T = \frac{P}{2}\frac{3}{2}\left\{\varphi_f i_q + \left(L_q - L_d\right)i_d i_q\right\} \tag{1}$$

Step 3.1. Determination of the Motor Size

The size of the motor should be chosen to satisfy the design goals. There are two steps for determining the motor size.

The first step is approximating the motor size theoretically. The volume of the rotor can be determined using Equation (2):

$$T = 2V_r \sigma \tag{2}$$

where T is the mechanical torque, V_r is the rotor volume, and σ is the shear stress. The rotor outer diameter can be calculated using Equation (3):

$$D = \sqrt{\left((4V_r)/\pi l\right)} \tag{3}$$

where D is the rotor outer diameter, V_r is the rotor volume and l is the axial length of the motor. The average diameter of the rotor can be approximated using Equation (4):

$$T = -\left(\frac{poles}{2}\right)\left(\frac{\mu_0 \pi D l}{2g}\right)B_g Fsin\delta_m \tag{4}$$

where l is the axial length, g is the radial distance of the air gap, B_g is the air gap flux density, and $Fsin\delta_m$ denotes the magnetomotive force wave as a function of the angle around the periphery.

In the second step, the JMAG Express program, which was used in the first step for design, verifies the results derived from the first step. This allows an approximate size for the motor that satisfies the design objective characteristics to be selected. Thus, we selected a rotor diameter of 260 mm, an axial length of 130 mm, a radial distance for the air gap of 1 mm, and an external diameter for the stator of 400 mm.

Step 3.2. Pole–Slot Number Selection

When determining the numbers of poles and slots, following conditions should be considered. The number of magnet poles is chosen using Equation (5):

$$p = \frac{60f}{N_s} \tag{5}$$

where p is the number of poles, f is the supply frequency, and N_s is the synchronous speed.

For heavy vehicles, selecting the largest possible pole number for low-velocity high-torque performances is recommended. Owing to the restrictions of the motor size, and leakage inductance, the appropriate pole-number for traction motors in heavy-duty vehicles is eight. When determining the number of slots, the high harmonics between rotor and stator should be considered. Preventing the demagnetization caused by the heating inside the permanent magnet due to iron loss and harmonics requires a high number of slots per pole per phase (q). For 24 slots, i.e., q = 1, there are high slot harmonics in the fifth and seventh harmonics. Therefore, we employed 48 slots, i.e., q = 2 [20–23].

Step 3.3. Determination of the Winding Method

Traction motors are generally conducted by high operational current that the turn number should be low, meaning that the cross-sectional area of a winding is high, and the inductance is very low. Using a distributed winding makes it possible to use the high torque generated by the difference of q and d axis inductances and create a back EMF sinusoidal waveform. Thus, the winding method was determined as a single-layer series with a distributed method [24–26].

Step 3.4. Rotor Topology Optimization

An IPMSM is distinguished by the arrangement of magnets. Compared to the most basic straight bar-type arrangement, a multi-layer magnetic array produces a large difference of the inductances along the d and q axes, which increases the reluctance torque [27]. A V-shaped arrangement makes a large region of permanent magnets per pole to be established, which can centralize the flux at the middle of the poles [28]. This increases the peak air gap flux density and produces a back EMF waveform that is close to a sine wave [29,30]. Moreover, it could raise the magnetic saliency to increase the incidence of the reluctance torque because the angle and length of the magnets can be adjusted to ensure a sufficient flux path along the q axis [31,32].

An IPMSM generates torque when the magnetic flux from the rotor's permanent magnet is linked to the windings of the stator. However, some magnetic fluxes do not face toward the stator, and the flux inside the rotor flows through the bridge via the shortest path, which is referred to as leakage flux. The bridge is designed to be purposely saturated to suppress flux leakage, and the firmness should be considered when deciding the thickness. Additionally, the flux barrier consists of a cavity which is

needed to reduce the harmonic components of the torque, thus reducing the ripple and increasing the power factor [33,34].

The cogging torque is a crucial factor that affects a number of troubles, including the torque ripple, the control inaccuracy of the motors, induced vibration, acoustic noise, and the speed ripple [35–38]. A step skew method has been reported that stacks the core by rotating it axially that reduces the cogging torque [39]. If skew is applied to the stator, manufacturing is more difficult and the winding is compromised, so the rotor can be twisted and stacked to achieve the same effect as the stator skew [40]. The symmetrical structure of the motor means that the EMF typically has odd-order harmonics. In three-phase machines, torque ripple mainly occurs in 6n-th-order harmonics. In this model, the 12th harmonic component of the cogging torque is very large. Therefore, this study applies step skew to reduce the 11th and 13th harmonic components of the EMF and the 12th harmonic of the cogging torque. The rotating angle is calculated using Equation (6):

$$\text{Skew Angle} = \frac{360°/h}{2^{n-1}} = \frac{360°/12}{2^2} = 7.5° \tag{6}$$

where h is the harmonic order of the cogging torque to be removed, and n is the step skew number.

In this study, the rotor was stacked by rotating it twice at 7.5°. The improvement of the back EMF waveform and the reduction in the cogging torque by applying step skew is discussed further in Step 4.1.

Step 4.1. No-Load Analysis

With no-load analysis, we can obtain the back EMF, air gap flux density, and the cogging torque generated by the rotor's rotation without an applied load current. This analysis was done at a base speed of 2000 rpm. The back EMF was the voltage induced upon unloading. The Fourier transform of the back EMF waveform allows the harmonics to be calculated. Figure 3 illustrates the waveform of the back EMF and Figure 4 displays the high-order harmonics distribution of the back EMF. The THD of the back EMF is calculated using Equation (7):

$$\text{THD} = \frac{\sqrt{V_2{}^2 + V_3{}^2 + V_4{}^2 \cdots}}{V_1} \times 100(\%) \tag{7}$$

where V_n represents the voltage of the n-th-order harmonic and V_1 is the voltage of the fundamental frequency.
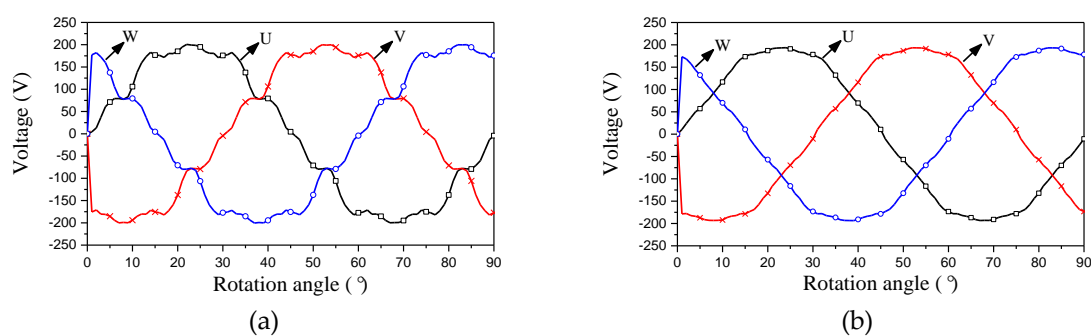

Figure 3. Analysis results for the back electromotive force (EMF) of (**a**) the non-skewed and (**b**) the skewed models.
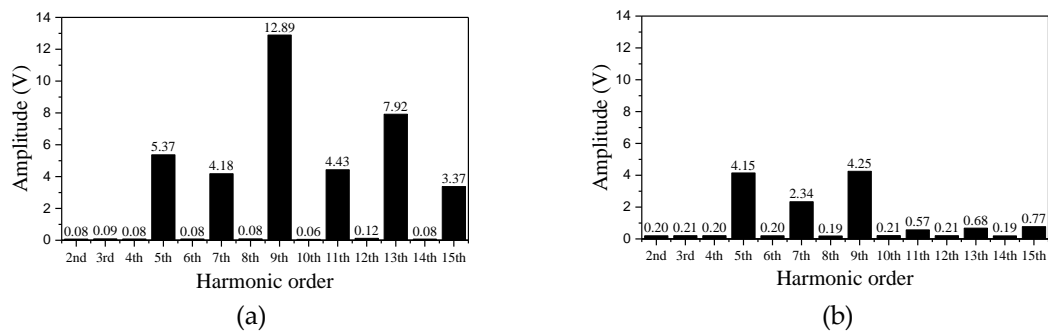
Figure 4. High-order harmonics distribution of the back EMF of (**a**) the non-skewed and (**b**) the skewed models.

The THD of the non-skewed model is approximately 15.86%, and this is reduced to 3.91% in the skewed model, which is approximately 25% that of conventional motors. A small THD indicates that the waveform is close to a sine wave and corresponds to a reduction in the peak current, heating, emissions, and core loss in the motor.

The air-gap is used as a free space where relative motion is possible between the stator and rotor.

The cogging torque is produced by interaction between the stator teeth and the permanent magnets of the rotor. It is generated when the rotor rotates. Figures 5 and 6 compare the cogging torque before and after the step skew structure is employed. The cogging torque of the non-skewed model is approximately 8 Nm, and this is reduced to 1.4 Nm in the skewed model, which is approximately 20% that of conventional motors.
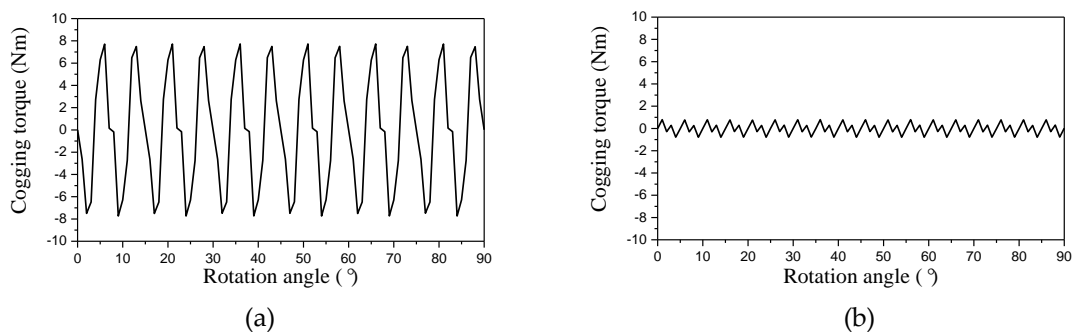

Figure 5. Analysis results for the cogging torque of (**a**) the non-skewed and (**b**) the skewed models.
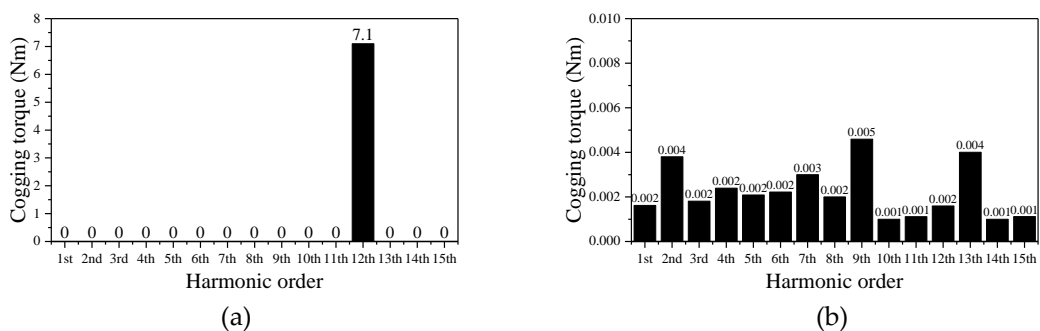

Figure 6. High-order harmonics distribution of the cogging torque of (**a**) the non-skewed and (**b**) the skewed models.

Step 4.2. Load Analysis

With load analysis, the torque, power, and speed range are examined according to changes in the load in the designed motor. The control of the motor was carried out within the voltage limit of $490V_{dc}$ and the base speed (2000 rpm) was determined by the voltage limit. At speeds under the base speed, the motor was controlled through MTPA (maximum torque per ampere) control. At speeds above the base speed, the characteristics of the motor were analyzed by the flux weakening control. Flux weakening control is a control method that increases the d axis current through phase angle control of the current to reduce the effective magnetic flux by permanent magnets. The analysis is conducted with a base speed of 2000 rpm under the rated current load (200 A) and the maximum current load (420 A).

The torque characteristics are analyzed by changing the phase angle of the current, and the torque ripple is calculated using Equation (8) [41]:

$$Torque \; ripple = \frac{T_{max} - T_{min}}{T_{ave}} \times 100 \; (\%) \tag{8}$$

where T_{max} is the maximum torque, T_{min} is the minimum torque, and T_{ave} is the average torque.

In Figure 7a, the highest torque under the rated current load is 651 Nm at a phase angle of 42°, with the torque ripple calculated to be 3.2% (Table 1).
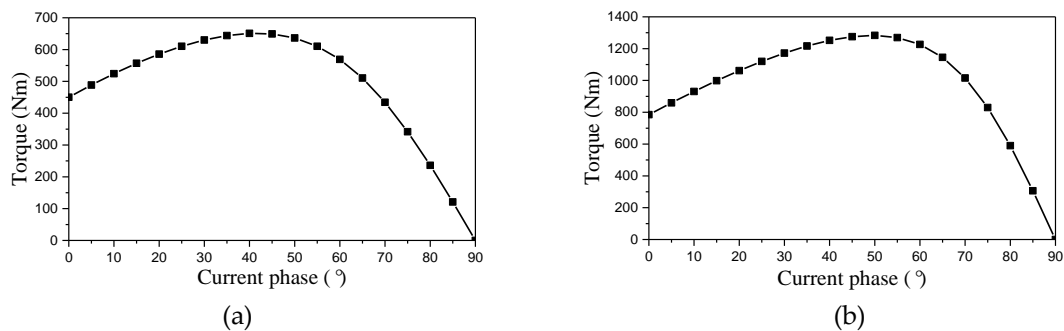

(a)   (b)

Figure 7. FEM analysis of the torque according to the current phase under (**a**) the rated current (200A) and (**b**) the maximum current (420A).

Table 1. Torque ripple under the rated and maximum current.

Current (A)	Average Torque (Nm)	Torque Ripple (%)
200	651.8	3.2
420	1277.87	3.5

The torque characteristics under the maximum current were analyzed in the same way as for the rated current. Figure 7b shows that a maximum torque of 1277.87 Nm is obtained at a phase angle of 50°, while Table 1 presents the calculated torque ripple at this angle, which is low at 4.1%. Figure 8 presents the FEM analysis results for the distribution of magnetic flux density. When the peak current is applied, the maximum flux density of the stator teeth and the yoke are 1.96 and 1.98 T, respectively, and the highest flux density is < 2 T.
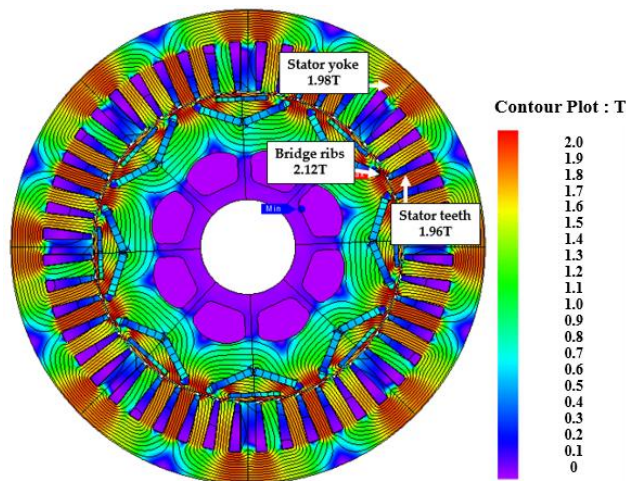
Figure 8. FEM analysis of the magnetic flux density distribution at the maximum current.

The FEM analysis was conducted under a voltage limit of 490 DC volts. The speed–torque–power characteristics produce a wide speed range of up to 9000 rpm (Figure 9a) [42–44]. The motor efficiency is calculated using Equations (9)–(11) [45–47]:

$$Efficiency = \frac{\omega T}{\omega T + P_{copper} + P_{core}} \times 100 \; (\%) \tag{9}$$

$$P_{copper} = 3I_p^2 R_p \tag{10}$$

$$P_{core} = P_{hysterisis} + P_{eddy} = K_h f B_{max}^2 + K_e f^2 B_{max}^\alpha \tag{11}$$

where ω and T represent the rotational speed and torque. P_{copper} represents the copper loss in the stator coil, and I_p *and* R_p are the phase current and resistance of the coil. P_{core} represents the core loss (iron loss), $P_{hysterisis}$, P_{eddy}, f, B_{max} are the hysteresis loss, eddy current loss, frequency, and the peak value of the flux density, respectively, and α, K_h, and K_e are constants.
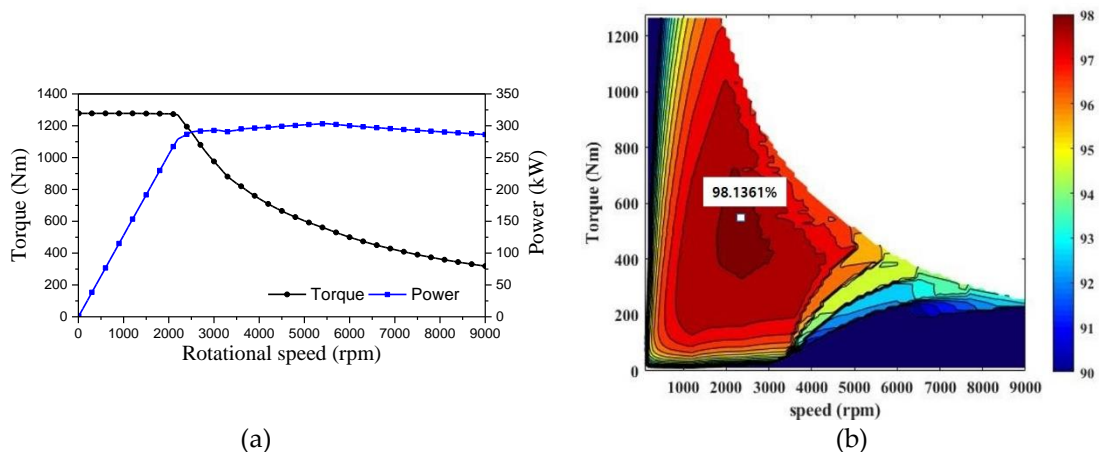

(a)

(b)

Figure 9. FEM analysis results for (**a**) the torque–speed and the power–speed characteristics and (**b**) the efficiency map.

In the FEM analysis, the copper loss of the windings and core loss are considered as losses for the motor. The efficiency map presented in Figure 9b was obtained by calculating the losses at operating points. The maximum efficiency (98.1361%) was obtained at 2400 rpm and 595.32 Nm.

Step 5. Mechanical Analysis

Mechanical stability is analyzed in accordance with the maximum stress to determine the mechanical stability at 6000 rpm, the design target. This motor uses 50JN470 steel as core material and N38UH (Neodymium: Nd-Fe-B) magnet as magnetic material. N38UM has a mechanical strength of Vickers hardness in 600 Hv, higher than the core material of 50JN470's hardness in 153 Hv. The Young's modulus of the rotor core is 165,000 MPa and the mass density of the rotor core is 7.7 kg/m^3. The von Mises stress distribution illustrated in Figure 10a shows that the peak stress of the rotor when rotating at 7200 rpm is delivered at the ribs, located near the magnets at 98.0873 MPa. When the motor is operated at the highest speed, the peak stress of the motor is lower than the yield point of the material in the rotor core (285 MPa) and the Vickers hardness of the rotor core. As shown by the change in von Mises stress according to the rotational speed (Figure 10b), mechanical stability is maintained up to 12,000 rpm. Therefore, the stress at the highest speed of 6000 rpm, which is the design goal, is about 35% of the yield point of the steel, while mechanical stability is confirmed in terms of the safety factor (2.0–2.5) suggested by Joseph P. Vidosic [48].
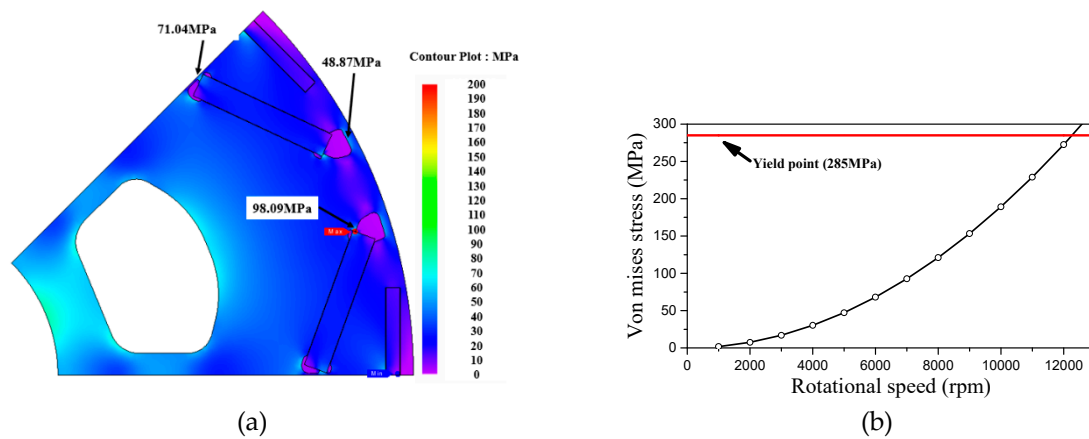

(a)   (b)

Figure 10. Mechanical analysis results for (**a**) the von Mises stress distribution in the rotor at 7200 rpm and (**b**) the alteration in the von Mises stress according to the rotational speed.

Step 6. Experimental Verification

A prototype of the traction motor designed using FEM analysis was manufactured and tested. Figure 11a presents an image of the IPM traction motor installed for testing, and Figure 11b depicts the entire test platform. The performance of the motor was verified by testing the maximum torque, maximum power, and maximum controllable rotational speed generated when the maximum current controlled through the inverter was applied to the motor.
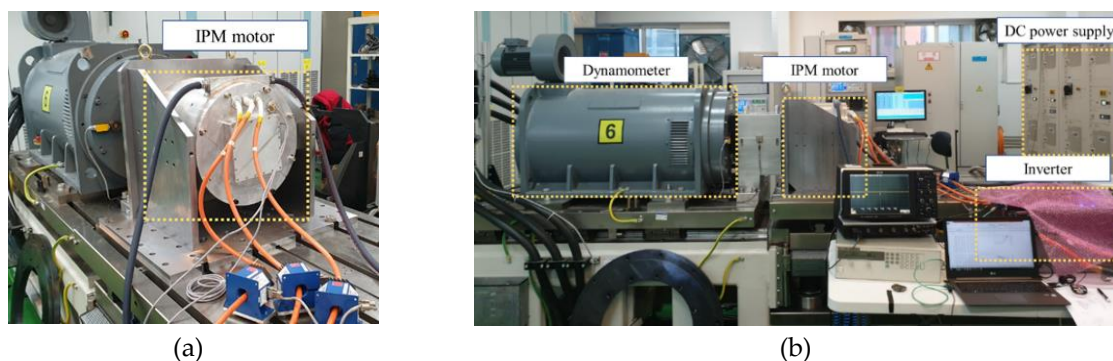

(a)   (b)

Figure 11. The picture of (**a**) a prototype of the designed motor and (**b**) the test platform for the motor.

When rotating at 1000 rpm, the back EMF measured by the oscilloscope was a maximum of 113.5 V, and a minimum of 113.7 V. This differs by about 5% from the value of a maximum of 120.6594 V, and a minimum of −120.671V, which is the back EMF obtained through the FEM analysis. As illustrated in Figure 12a, the highest torque from the experimental data was 1267.54 Nm, which is about 1% lower than the FEM analysis results (1277.87 Nm), while the base speed at which the flux weakening control was initiated by the voltage limit is almost the same at 2000 rpm. However, mechanical losses and an increase in temperature, which are not considered in the FEM analysis, mean that ideal flux weakening control at speeds >6000 rpm is not possible. Figure 12a,b show that the maximum torque was 1267.54 Nm, the maximum power was 277 kW, and the maximum speed was 6000 rpm in the experimental testing. Figure 13a,b compares the FEM analysis and the experimental results in terms of changes in the torque and power according to the applied current at a base speed of 2000 rpm. The experimental results differ by about 1% from the FEM results due to the mechanical and inverter losses that are not considered in the FEM analysis. Figure 14 displays the efficiency map of the motor as measured experimentally. An efficiency test was conducted intensively near base speed and not at speeds above 3500 rpm because IPM motors have high efficiency characteristics near base speed. It was conducted at speeds of 500, 1000, 1500, 1600, 1700, 1800, 1900, 2000, 2100, 2200, 2300, 2400, 2500, 3000, 3500 rpm, and load currents at 100, 200, 300, 400, and 420 A. The maximum efficiency of the motor was 96.012% at 1600 rpm with an input current of 100 A. This is about 2% lower than the results from the FEM analysis, which only considers the iron and copper losses of the motor.
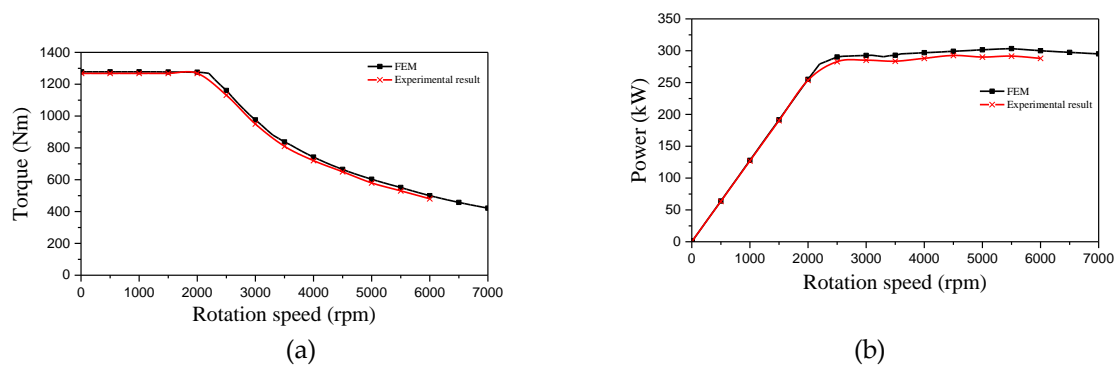

(a)   (b)

Figure 12. FEM analysis and experimental results for (**a**) the torque and (**b**) the power according to the rotational speed.
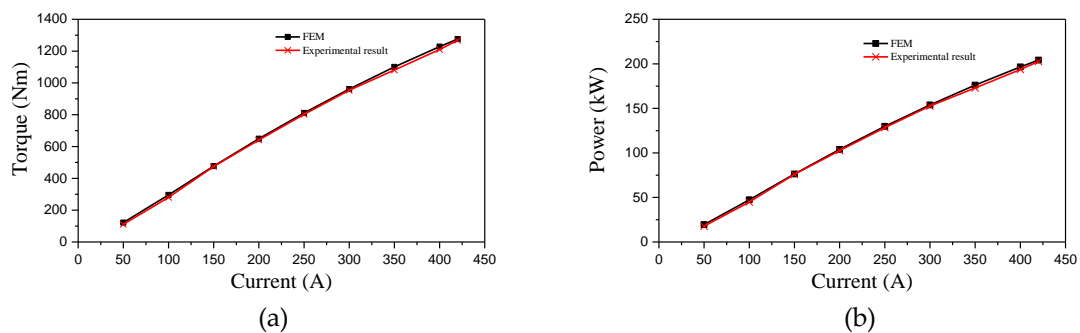

(a)   (b)

Figure 13. FEM analysis and experimental results at a base speed of 2000 rpm for (**a**) the torque and (**b**) the power according to the rotational speed.
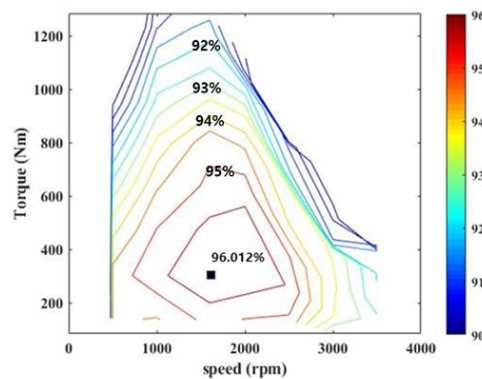
Figure 14. Efficiency map derived from the experimental data.

Step 7. Determining the Specifications of the Designed Motor

Tables 2 and 3 show the parameters and characteristics of the designed traction motor. Traction motors for heavy-duty vehicles require outstanding performance when compared to motors for other EVs, including high torque, power, mechanical strength, and efficiency, as well as a large speed range. Therefore, the design target was to accomplish a high torque of 1200 Nm, a high power of 250 kW, and a wide operating speed range of 6000 rpm without enlarging the size. The motor was designed using FEM analysis and verified by experiment. The experimental results reveal a peak torque of 1267.54 Nm, a highest power of 285.07 kW, and a maximum efficiency of 96.01% at a speed range of 6000 rpm.

Table 2. Parameters of the designed traction motor.

Components	Parameters	Target
Stator	Slots number	48
	Outer diameter (mm)	400
	Inner diameter (mm)	262
Winding	Turns number (turn)	5
	Coil resistance (Ω)	0.01178
Rotor	Poles number	8
	Outer diameter (mm)	260
	Inner diameter (mm)	80
	Skew angle (°)	7.5
Motor	Axial length (mm)	130
	Iron core material	50JN470
	Permanent magnet material	N39UH (Nd-Fe-B Magnet)
	Remanence of PM (T)	1.23
	Current density (A/mm^2)	10.4
	Cooling method	Water cooling

Table 3. Characteristics of the designed traction motor.

Characteristics	FEM Results	Experiment Results
Maximum torque (Nm)	1277.87	126,754
Maximum power (kW)	303.09	285.07
Maximum efficiency (%)	98.13	96.01
Maximum speed (rpm)	9000	6000
Maximum voltage (V_{dc})	490	490

3. Conclusions

This paper is noteworthy in that it develops a high-torque, high-speed traction motor for heavy-duty vehicles. Given the global trend toward eco-friendly systems, the electrification of heavy-duty vehicles, which traditionally emit significant levels of pollution, is becoming an important research focus. This research is also meaningful in that this traction motor, which can be universally employed in buses and trailers, was verified using both FEM and experimental analysis. To ensure a high torque, the interior magnets of the rotor are arranged in a delta array. Furthermore, the rotor core is divided into three stacks and step skew is employed to remove the harmonics of the back EMF so that it can run over a wide speed range by reducing the THD and the peak value of the induced voltage. The skew angle was selected to remove the specific harmonic components of the cogging torque, thus reducing the cogging torque to 20% of that of conventional motors.

The traction motor designed in this paper can be used simply by converting the gearbox of heavy commercial vehicles that require high torque, such as buses, trailers, and heavy lorries. Therefore, the designed motor can reduce costs by maximizing its mass production potential and reducing the development time for EVs. The design process employed for the proposed motor can also reduce the time and cost of designing and developing various electric machines and traction motors.

Author Contributions: Conceptualization, D.-K.L. and J.-S.R.; methodology, D.-K.L. and J.-S.R.; software, D.-K.L.; validation, D.-K.L. and J.-S.R.; formal analysis, D.-K.L.; investigation, D.-K.L.; resources, D.-K.L.; data curation, D.-K.L.; writing—original draft preparation, D.-K.L.; writing—review and editing, D.-K.L. and J.-S.R.; visualization, D.-K.L.; supervision, J.-S.R.; project administration, D.-K.L. and J.-S.R.; funding acquisition, J.-S.R. All authors have read and agreed to the published version of the manuscript.

Conflicts of Interest: The authors declare no conflict of interest.

References

1. Yu, D.; Huang, X.; Fang, Y.; Zhang, J. Design and comparison of interior permanent magnet synchronous traction motors for high speed railway applications. In Proceedings of the 2017 IEEE Workshop on Electrical Machines Design, Control and Diagnosis, Nottingham, UK, 20–21 April 2017; pp. 58–62.
2. Raihan, M.A.H.; Smith, K.J.; Almoraya, A.A.; Khan, F. Interior permanent magnet synchronous machine (IPMSM) design for environment friendly hybrid electric vehicle (HEV) applications. In Proceedings of the 2017 IEEE Region 10 Humanitarian Technology Conference (R10-HTC), Dhaka, Bangladesh, 21–23 December 2017; pp. 375–378.
3. Ma, F.; Yin, H.; Wei, L.; Tian, G.; Gao, H. Design and Optimization of IPM Motor Considering Flux Weakening Capability and Vibration for Electric Vehicle Applications. *Sustainability* **2018**, *10*, 1533. [CrossRef]
4. Bitar, Z.; Al Jabi, S. Studying the Performances of Induction Motor Used in Electric Car. *Energy Procedia* **2014**, *50*, 342–351. [CrossRef]
5. Yang, Z.; Shang, F.; Brown, I.P.; Krishnamurthy, M. Comparative Study of Interior Permanent Magnet, Induction, and Switched Reluctance Motor Drives for EV and HEV Applications. *IEEE Trans. Transp. Electrif.* **2015**, *1*, 245–254. [CrossRef]
6. Wang, J.; Xia, Z.P.; Howe, D. Three-Phase Modular Permanent Magnet Brushless Machine for Torque Boosting on a Downsized ICE Vehicle. *IEEE Trans. Veh. Technol.* **2005**, *54*, 809–816. [CrossRef]
7. Kawano, S.; Murakami, H.; Nishiyama, N.; Ikkai, Y.; Honda, Y.; Higaki, T. High performance design of an interior permanent magnet synchronous reluctance motor for electric vehicles. In Proceedings of the Power Conversion Conference—PCC'97, Nagaoka, Japan, 6 August 2002; Volume 1, pp. 33–36.
8. Kim, K.-T.; Kim, K.-S.; Hwang, S.-M.; Kim, T.-J.; Jung, Y.-H.; Tae-Jong, K. Comparison of magnetic forces for IPM and SPM motor with rotor eccentricity. *IEEE Trans. Magn.* **2001**, *37*, 3448–3451.

9.   Han, J.-H.; Ryu, G.-H.; Lee, K.-D.; Lee, J.-J.; Kim, I.-G.; Jeong, T.-C.; Kim, W.-H.; Lee, J. Optimization in structural design of triangle type IPMSM of permanent magnetic rotor using Box-Behnken methodology. In Proceedings of the 2012 15th International Conference on Electrical Machines and Systems (ICEMS), Sapporo, Japan, 21–24 October 2012; pp. 2–5.

10.   Yeo, H.-K.; Ro, J.-S. Novel Analytical Method for Overhang Effects in Surface-Mounted Permanent-Magnet Machines. *IEEE Access* **2019**, *7*, 148453–148461. [CrossRef]

11.   Lee, Y.-S.; Kim, K.-T.; Park, J.-H.; Lee, S.-J.; Chung, T.-K.; Ro, J.-S. Characteristic analysis and design of novel high-frequency shell-type coaxial transformer. *IET Electr. Power Appl.* **2019**, *13*, 2027–2034. [CrossRef]

12.   Khan, S.; Bukhari, S.S.H.; Ro, J.-S. Design and Analysis of a 4-kW Two-Stack Coreless Axial Flux Permanent Magnet Synchronous Machine for Low-Speed Applications. *IEEE Access* **2019**, *7*, 173848–173854. [CrossRef]

13.   Liu, G.; Xu, G.; Zhao, W.; Du, X.; Chen, Q. Improvement of Torque Capability of Permanent-Magnet Motor by Using Hybrid Rotor Configuration. *IEEE Trans. Energy Convers.* **2017**, *32*, 953–962. [CrossRef]

14.   Yang, Y.; Castano, S.M.; Yang, R.; Kasprzak, M.; Bilgin, B.; Sathyan, A.; Dadkhah, H.; Emadi, A. Design and Comparison of Interior Permanent Magnet Motor Topologies for Traction Applications. *IEEE Trans. Transp. Electrif.* **2016**, *3*, 86–97. [CrossRef]

15.   Rashidaee, S.; Gholamian, S.A. Reduction of Cogging Torque in IPM Motors by Using the Taguchi and Finite Element Method. *Int. J. Comput. Sci. Eng. Surv.* **2011**, *2*, 1–10. [CrossRef]

16.   Mun, J.-M.; Park, G.-J.; Seo, S.; Kim, D.-W.; Kim, Y.-J.; Jung, S.-Y. Design Characteristics of IPMSM with Wide Constant Power Speed Range for EV Traction. *IEEE Trans. Magn.* **2017**, *53*, 1. [CrossRef]

17.   Zhang, J.; Wen, X.; Wang, Y.; Li, W. Modeling and analysis of nonlinear interior permanent magnet synchronous motors considering saturation and cross-magnetization effects. In Proceedings of the 2016 IEEE Transportation Electrification Conference and Expo, Asia-Pacific (ITEC Asia-Pacific), Busan, Korea, 1–4 June 2016; pp. 611–615.

18.   Liu, Y.-X.; Li, L.; Cao, J.-W.; Sun, Z.; Sun, Z.-Y.; Zhang, J.-P. The Optimization Design of Short-Term High-Overload Permanent Magnet Motors Considering the Nonlinear Saturation. *Energies* **2018**, *11*, 3272. [CrossRef]

19.   Gabdullin, N.; Ro, J.-S. Novel Non-Linear Transient Path Energy Method for the Analytical Analysis of the Non-Periodic and Non-Linear Dynamics of Electrical Machines in the Time Domain. *IEEE Access* **2019**, *7*, 37833–37854. [CrossRef]

20.   Sim, M.-S.; Ro, J.-S. Analysis of an eddy current brake for an actuator of a high-voltage direct current circuit breaker. *IET Electr. Power Appl.* **2019**, *13*, 1387–1391. [CrossRef]

21.   Ştirban, A.; Tutelea, L.; Iles-Klumpner, D.; Boldea, I. FEM analysis of concentrated coils nonuniform slot (6+6/8) IPMSM fed with trapezoidal current. In Proceedings of the 11th International Conference on Optimization of Electrical and Electronic Equipment, Brasov, Romania, 22–24 May 2008; pp. 45–53.

22.   Zhu, Z.Q.; Wu, D.; Ge, X. Investigation of Voltage Distortion in Fractional Slot Interior Permanent Magnet Machines Having Different Slot and Pole Number Combinations. *IEEE Trans. Energy Convers.* **2016**, *31*, 1192–1201. [CrossRef]

23.   Ge, X.; Zhu, Z.Q. Sensitivity of Manufacturing Tolerances on Cogging Torque in Interior Permanent Magnet Machines With Different Slot/Pole Number Combinations. *IEEE Trans. Ind. Appl.* **2017**, *53*, 3557–3567. [CrossRef]

24.   Tangudu, J.K.; Jahns, T.M.; Bohn, T.P. Design, analysis and loss minimization of a fractional-slot concentrated winding IPM machine for traction applications. In Proceedings of the 2011 IEEE Energy Conversion Congress and Exposition, Phoenix, AZ, USA, 17–22 September 2011; pp. 2236–2243.

25.   Gabdullin, N.; Ro, J.-S. Energy-Efficient Eco-Friendly Zero-Holding-Energy Magnetic Contactor for Industrial and Vehicular Applications. *IEEE Trans. Veh. Technol.* **2020**, *69*, 5000–5011. [CrossRef]

26.   Lim, M.-S.; Chai, S.-H.; Hong, J.-P. Design of Saliency-Based Sensorless-Controlled IPMSM with Concentrated Winding for EV Traction. *IEEE Trans. Magn.* **2015**, *52*, 1–4. [CrossRef]

27.   Alsawalhi, J.Y.; Sudhoff, S.D. Design Optimization of Asymmetric Salient Permanent Magnet Synchronous Machines. *IEEE Trans. Energy Convers.* **2016**, *31*, 1315–1324. [CrossRef]

28. Lee, K.-D.; Lee, J.; Lee, H.W. Inductance Calculation of Flux Concentrating Permanent Magnet Motor through Non-Linear Magnetic Equivalent Circuit. *IEEE Trans. Magn.* **2015**, *51*, 1.

29. Liang, J.; Parsapour, A.; Yang, Z.; Caicedo-Narvaez, C.; Moallem, M.; Fahimi, B. Optimization of Air-Gap Profile in Interior Permanent-Magnet Synchronous Motors for Torque Ripple Mitigation. *IEEE Trans. Transp. Electrif.* **2019**, *5*, 118–125. [CrossRef]

30. Maema, A.; Shimomura, S.; Kono, M. Mathematical model considering air gap space harmonics in IPMSM. In Proceedings of the 19th International Conference on Electrical Machines and Systems (ICEMS), Chiba, Japan, 13–16 November 2016; pp. 1–6.

31. Honda, Y.; Higaki, T.; Morimoto, S.; Takeda, Y. Rotor design optimisation of a multi-layer interior permanent-magnet synchronous motor. *IEE Proc. Electr. Power Appl.* **1998**, *145*, 119. [CrossRef]

32. Gabdullin, N.; Ro, J.-S. Analysis of Nonlinear Dynamics of Permanent Magnet Magnetic Contactor via Novel Computationally Efficient Analytical Method Considering Stray and Leakage Fluxes. *IEEE Access* **2020**, *8*, 57273–57282. [CrossRef]

33. Guan, B.; Zhao, Y.; Ruan, Y. Torque Ripple Minimization in Interior PM Machines using FEM and Multiple Reference Frames. In Proceedings of the 2006 1ST IEEE Conference on Industrial Electronics and Applications, Singapore, 24–26 May 2006; pp. 1–6.

34. Jung, Y.-H.; Lim, M.-S.; Yoon, M.-H.; Jeong, J.-S.; Hong, J.-P. Torque Ripple Reduction of IPMSM Applying Asymmetric Rotor Shape under Certain Load Condition. *IEEE Trans. Energy Convers.* **2018**, *33*, 333–340. [CrossRef]

35. Luu, P.T.; Lee, J.-Y.; Hwang, W.; Woo, B.-C. Cogging Torque Reduction Technique by Considering Step-Skew Rotor in Permanent Magnet Synchronous Motor. In Proceedings of the 2018 21st International Conference on Electrical Machines and Systems (ICEMS), IEEE, Jeju, South Korea, 7–10 October 2018; pp. 219–223.

36. Kim, T.-W.; Chang, J.-H. Influence of Cogging Torque Reduction Method on Torque Ripple in a Surface-Mounted Permanent Magnet Synchronous Motor. *J. Magn.* **2012**, *17*, 109–114. [CrossRef]

37. Gomez, D.J.; Tovar-Barranco, A.; Rodriguez, A.L.; Lopez-De-Heredia, A.; Villar, I. On-load cogging torque calculation using Frozen Permeability method and permeance network models. In Proceedings of the 2016 XXII International Conference on Electrical Machines (ICEM), IEEE, Lausanne, Switzerland, 4–7 September 2016; pp. 499–505.

38. Zhang, G.; Yu, W.; Hua, W.; Cao, R.; Qiu, H.; Guo, A. The Design and Optimization of an Interior, Permanent Magnet Synchronous Machine Applied in an Electric Traction Vehicle Requiring a Low Torque Ripple. *Appl. Sci.* **2019**, *9*, 3634. [CrossRef]

39. Kim, T.-W.; Chang, J.-H. Effective step-skew method for cogging torque reduction in surface-mounted permanent magnet synchronous motor. *J. Korean Phys. Soc.* **2013**, *63*, 288–292. [CrossRef]

40. Ge, X.; Zhu, Z.Q.; Kemp, G.; Moule, D.; Williams, C. Optimal step-skew methods for cogging torque reduction accounting for three-dimensional effect of interior permanent magnet machines. *IEEE Trans. Energy Convers.* **2017**, *32*, 222–232. [CrossRef]

41. Chen, Q.; Xu, G.; Liu, G.; Zhao, W.; Liu, L.; Lin, Z. Torque Ripple Reduction in Five-Phase IPM Motors by Lowering Interactional MMF. *IEEE Trans. Ind. Electron.* **2018**, *65*, 8520–8531. [CrossRef]

42. Kato, T.; Matsuura, T.; Sasaki, K.; Tanimoto, T. Principle of variable leakage flux IPMSM using arc-shaped magnet considering variable motor parameter characteristics depending on load current. In Proceedings of the 2017 IEEE Energy Conversion Congress and Exposition (ECCE), Cincinnati, OH, USA, 1–5 October 2017; pp. 5803–5810.

43. Honda, Y.; Nakamura, T.; Higaki, T.; Takeda, Y. Motor design considerations and test results of an interior permanent magnet synchronous motor for electric vehicles. In Proceedings of the IAS '97, Conference Record of the 1997 IEEE Industry Applications Conference Thirty-Second IAS Annual Meeting, New Orleans, LA, USA, 5–9 October 1997; Volume 1, pp. 75–82.

44. Zhang, Y.; Cao, W.; McLoone, S.; Morrow, D.J. Design and Flux-Weakening Control of an Interior Permanent Magnet Synchronous Motor for Electric Vehicles. *IEEE Trans. Appl. Supercond.* **2016**, *26*, 1–6. [CrossRef]

45. Okamoto, S.; Denis, N.; Kato, Y.; Ieki, M.; Fujisaki, K. Core Loss Reduction of an Interior Permanent-Magnet Synchronous Motor Using Amorphous Stator Core. *IEEE Trans. Ind. Appl.* **2016**, *52*, 2261–2268. [CrossRef]

46. Yamazaki, K.; Seto, Y. Iron loss analysis of interior permanent magnet synchronous motors variation of main loss factors due to driving condition. *IEEE Int. Conf. Electr. Mach. Driv.* **2005**, *42*, 1633–1638.

47. Mahmoud, H.; Bacco, G.; Degano, M.; Bianchi, N.; Gerada, C. Synchronous Reluctance Motor Iron Losses: Considering Machine Nonlinearity at MTPA, FW, and MTPV Operating Conditions. *IEEE Trans. Energy Convers.* **2018**, *33*, 1402–1410. [CrossRef]

48. Cha, K.-S.; Kim, D.-M.; Park, M.-R.; Yoon, M.-H.; Hong, J.-P. Multipolar High-Speed IPMSM Design for EV Traction Considering Mechanical Stress. In Proceedings of the 2016 IEEE 84th Vehicular Technology Conference (VTC-Fall), Montreal, QC, Canada, 18–21 September 2016; pp. 1–6.